Optics Communications 383 (2017) 378–385

Contents lists available at ScienceDirect

Optics Communications

journal homepage: www.elsevier.com/locate/optcom

Practical retrace error correction in non-null aspheric testing: A comparison

Tu Shi [a], Dong Liu [a,*], Yuhao Zhou [a], Tianliang Yan [a], Yongying Yang [a], Lei Zhang [a], Jian Bai [a], Yibing Shen [a], Liang Miao [b], Wei Huang [b]

[a] State Key Laboratory of Modern Optical Instrumentation, College of Optical Science and Engineering, Zhejiang University, Hangzhou 310027, China
[b] State Key Laboratory of Applied Optics, Changchun Institute of Optics, Fine Mechanics and Physics, Chinese Academy of Sciences, Changchun 130033, China

ARTICLE INFO

Article history:
Received 30 July 2016
Received in revised form
13 September 2016
Accepted 16 September 2016
Available online 22 September 2016

Keywords:
Asphere
Retrace error
Surface measurement
Figure
Interferometry

ABSTRACT

In non-null aspheric testing, retrace error forms the primary error source, making it hard to recognize the desired figure error from the aliasing interferograms. Careful retrace error correction is a must bearing on the testing results. Performance of three commonly employed methods in practical, i.e. the GDI (geometrical deviation based on interferometry) method, the TRW (theoretical reference wavefront) method and the ROR (reverse optimization reconstruction) method, are compared with numerical simulations and experiments. Dynamic range of these methods are sought out and the application is recommended. It is proposed that with aspherical reference wavefront, dynamic range can be further enlarged. Results show that the dynamic range of the GDI method is small while that of the TRW method can be enlarged with aspherical reference wavefront, and the ROR method achieves the largest dynamic range with highest accuracy. It is recommended that the GDI and TRW methods be applied to apertures with small figure error and small asphericity, and the ROR method for commercial and research applications calling for high accuracy and large dynamic range.

1. Introduction

Non-null aspheric testing is increasingly employed for its flexible and versatile measurement properties, especially for testing aspherics with large apertures, large departures or different parameters. By now, several non-null interferometric testing ways have been proposed, such as the SNI (sub-Nyquist interferometry) [1], the PCI (partially compensating interferometry) [2], the SSI (subaperture stitching interferometry) [3–5], the NASSI (non-null annular subaperture stitching interferometry) [6] and the TWI (Tilted Wave Interferometry) [7], etc. With non-null configurations, not only the aspheric testing range is enlarged, but also the time and costs are saved compared to the null configurations [8].

In a null test, rays impinge perpendicularly onto the test surface. However in a non-null arrangement, most rays impinge in directions that differ from the normals of the test part and travel through different paths from the origin after reflection, thus retrace error is induced [9,10]. In the final detected interferograms, fringe deformation caused by the retrace error is aliasing with that due to the aspheric figure error. Distinguishing these two major errors, that is, the retrace error correction, takes up the core algorithm in non-null aspheric test for the purpose of figure error extraction. An appropriated retrace error correction method directly impacts the accuracy of the testing results and the efficiency of the figure error reconstruction process.

Much effort has been put on this issue as listed in Table 1. Based on aberration expressions, Huang [11] derived the propagation errors due to non-common path through theoretical prediction. By empirically mapping the interferometer errors, Evans [12] proposed a correction method with aberration expansions and several measurements of a tilted off-axis flat in advance, reducing the error deviations from 150 nm to around 30 nm. It is applicable to "black box" systems but limited to low spatial frequency. With the third-order aberration theory, Murphy [13] presented a calibrating method. However, it not allows for full error characterization of the system and becomes sophisticated when imaging configuration is more than one singlet lens. For "black box" system correction, there are another two methods. One is the GDI (geometric deviation based on interferometry) method, which assumes the imaging system is perfect during the correction and is a common process in subaperture stitching tests [14]. The other is the perturbation method [15–17] that describes the interferometer with characteristic functions. Several priori measurements with the reference surface at different locations are required for system error calibration and figure error reconstruction based on the

* Corresponding author.
E-mail address: liudongopt@zju.edu.cn (D. Liu).

http://dx.doi.org/10.1016/j.optcom.2016.09.034
0030-4018/

Table 1
Retrace error correction methods for non-null aspheric testing.

Method	Based on	Model box	Prior knowledge
Huang	Aberration expansions	Black	Relative pupil positions
Evans			Several measurements of tilted flat off-axis
Murphy		White	Parameters of the imaging system
GDI	Perfect imaging	Black	shape of the incident reference sphere
Perturbation	Perturbation theory	Black	Calibration priori done with several measurements
Separate correction	Theoretical wavefront	White	System prescription, calibrated priori to the test
TRW			
ROR	Optimized matching	White	System prescription, calibrated priori to the test
Reverse ray tracing			
Reverse optimization			System prescription, calibrated during the test

perturbation theory. Limitation of this method in practice is mechanical stability and a need of higher-order correction to improve accuracy [15]. In order to further characterize the interferometer, "white box" model is employed, in which once or multiple ray tracing of the system is utilized for retrace error correction. As shown in Table 1, based on theoretical wavefront obtained by ray tracing the interferometer model once, system inherent retrace error is corrected with separate correction method [9] or TRW (theoretical reference wavefront) method [18]. To correct retrace error induced also by the figure error of the test part, the idea of optimized matching of data from system model and experiments with multiple ray tracing and optimization of the model is first presented by team of Greivenkamp, called the reverse optimization method [10,19]. Calibration of the system model is accomplished while solving the tested figure error. Considering that multiple measurements and iterations are needed with computationally intensive and long time, it is better for system calibration. Also based on optimized matching, the ROR method (reverse optimization reconstruction) [6,20] and reverse ray tracing method [21,22] correct retrace error on a calibrated interferometer model. The latter ray traces reversely from the detector to the test surface, while the other sequentially. Retrace error is almost completely corrected in ideal simulations of both cases. It is notable that for "white box" model, system calibration is very important and has been given much attention to [10,19,23–26].

In this paper, three practical methods, i.e. the GDI, TRW and ROR methods, are analyzed and compared with successive tested figure errors and non-null wavefronts to exhibit the performance trends and dynamic ranges, instead of specifically independent testing cases as reported in previous literatures. Dynamic ranges are sought out. It is suggested to employ aspherical reference wavefronts for dynamic range enlargement, which also does much favor to the calibration of "white box" system in the meantime if the generator of the test wave is singlet lens. Experiments are presented for demonstration and application of the three methods are recommended based on the analyses.

2. Algorithms

Assume that the figure error of the tested asphere is W_{asp}. In a certain non-null system, test wavefront carrying the information of W_{asp} coherences with the reference wavefront, forming the non-null interferogram which is then imaged onto the detector. By interferograms analyzation, the wavefront detected at image plane noted as W_{det} can be extracted, which is an aliasing of the information of W_{asp} and retrace error. With retrace error corrected, W_{asp} is able to be reconstructed from W_{det}.

2.1. The GDI method

It is known in a null test, OPD between the reference wave and the test wave is twice the W_{asp} if the incident rays reflect once on the test part. Figure error is obtained as half of the detected wavefront. As for non-null test, shape difference between reference wavefront and the tested asphere is not only W_{asp}, but also the geometric deviation (W_{gdv}) between reference wavefront and the nominal aspheric shape. With the GDI method, W_{asp} is obtained as

$$W_{asp} \approx \frac{1}{2}W_{det} - W_{gdv}. \tag{1}$$

To simplify the calculation of W_{gdv}, spherical reference wavefront is usually employed in actual applications. Assuming that the shape of the nominal asphere and the reference wavefront is $f(\rho)$ and $S(\rho)$ respectively at the radial coordinate ρ, Eq. (1) is written as

$$W_{asp} \approx \frac{1}{2}W_{det} - \left[f(\rho) - S(\rho)\right]\cdot \cos\alpha(\rho), \tag{2}$$

where $\alpha(\rho)$ represents for the normal angle of the asphere. As shown in Eq. (2), besides the nominal shape of the tested asphere, priori knowledge of the algorithm is the curvature radius of the spherical reference wavefront. It must be said that this algorithm is based on the assumption that the imaging system is perfect. Or in the strict sense, it solves the non-null problem the way of a null configuration.

2.2. The TRW method

Retrace error has much to do with the system structure, since most reflected rays propagate through parts of the optical elements that are different from those of the incident. Understanding how rays propagate in the system helps with a further correction. Aided by ray tracing program, interferometric system is able to be modeled and calibrated for a "white box" system to show the light paths of both the reference and test waves. Retrace error is corrected with the TRW method by ray tracing the interferometric system model once.

Suppose the actual system has been modeled and calibrated in a ray tracing program, in which the test part is modeled with its nominal shape. After ray tracing the model once, OPD on the image plane can be obtained, noted as W'_{det}. W'_{det} is called the theoretical wavefront, which expresses the inherent retrace error of the system. Since the model is according to the actual system, W_{det} on the detector deforms from W'_{det} due to the existence of the aspheric figure error to be tested. This situation is similar to a null test [18]. According to the coherence testing principle, aspheric figure error can be obtained as

$$W_{asp} \approx \frac{1}{2}(W_{det} - W'_{det}). \tag{3}$$

2.3. The ROR method

To further correct the additional retrace error which is unpredictable caused by the unknown aspheric figure error, the ROR method employs "white box" system modeling with multiple ray tracing to realize an optimized data matching. Similarly, the interferometric system is modeled and calibrated according to the real one except the test part. Assuming the deformation of the nominal asphere in the model is W^*_{asp} and the corresponding wavefront on the image plane obtained by ray tracing is W^*_{det}. W^*_{det} will be the same as W_{det} if W^*_{asp} is the same as the actual figure error W_{asp}. By changing W^*_{asp} to make W^*_{det} optimized matching W_{det}, the figure error induced retrace error is also taken into calculation at the same time with multiply iterative ray tracing. Both inherent and unpredictable retrace errors are corrected during this process. In order to map the figure error and the wavefront uniquely, orthogonal polynomials are advocated for characterizing of the concerned zones as

$$\begin{cases} W_{asp} \approx \sum_{i=1}^{M} B_i U_i, \quad W^*_{asp} \approx \sum_{i=1}^{M} B^*_i U_i, \\ W_{det} \approx \sum_{j=1}^{N} C_j V_j, \; W^*_{det} \approx \sum_{j=1}^{N} C^*_j V_j, \end{cases} \tag{4}$$

where U_i ($i = 1, 2, \cdots, M$) and V_j ($j = 1, 2, \cdots, N$) are orthogonal polynomials for figure error and wavefront expression, M and N are the total terms of the employed polynomials, B_i and C_j are the corresponding coefficients of W_{asp} and W_{det}, while B^*_i and C^*_j are those in the modeled system. Among these, C_j can be easily got via polynomials fitting of W_{det} and C^*_j can also be obtained via fitting W^*_{det}, which is acquired by ray tracing the model once. Setting B^*_i as variables, the change of B^*_i will result in a change of C^*_j. Trace the model iteratively after each round change of B^*_i according to the objective function, until C^*_j is close enough or optimized matching to C_j. The objective function is set up as

$$\begin{aligned} &W\left(\left[B^*_{1|o}, B^*_{2|o}, \cdots, B^*_{i|o}, \cdots, B^*_{M|o}\right]\right) \\ &= \min\left[\left(W^*_{det} - W_{det}\right)^2 + c\right] \\ &= \min\left[\sum_{j=1}^{N} \omega_j^2 \left(C^*_j - C_j\right)^2 + c\right], \end{aligned} \tag{5}$$

where $B^*_{i|o}$ is the optimal solution of B^*_i, ω_j^2 is the optimization weight and c is an additional constraint to restrict the solution space. The figure error is then reconstructed as

$$W_{asp} \approx W^*_{asp} \approx \sum_{i=1}^{M} B^*_{i|o} U_i. \tag{6}$$

3. Simulation analyses and comparisons

Numerical experiments are executed to evaluate the performances of the GDI, TRW and ROR methods of retrace error correction for non-null aspheric testing. In the simulations, the methods are applied to aspherics with only one circular aperture. For sub-aperture stitching tests, the retrace error correction process of each aperture is the same as the case of one circular aperture.

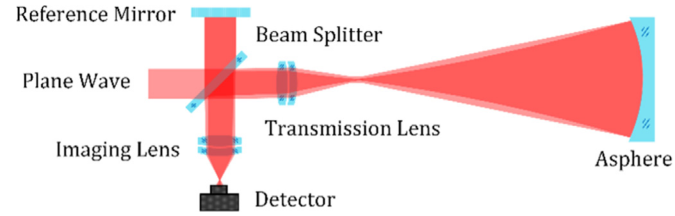

Fig. 1. System layout for non-null aspheric testing.

A Twyman-Green interferometric system with laser wavelength of λ=632.8 nm is employed to carry out the simulations. Fig. 1 shows the system layout, in which the incident plane wave is divided into two by the beam splitter. One wave is reflected by the reference mirror serving as the reference wave. The other in the test arm propagates through the transmission lens and is transformed into a wavefront that is different from the nominal aspheric shape, forming the non-null condition. Reflected by the asphere, the test wave then interferes with the reference one at the beam splitter. Interferogram is then imaged onto the detector by imaging lens. Since absolutely accurate adjustment can never come true in practice but the system can be carefully adjusted and modeled [10,18,23–26], the dominant aberration terms will be the primary aberrations. Therefore, the simulation results in this section are also preprocessed with the primary aberrations corrected.

3.1. Retrace error correction in different non-null degrees

Greater non-null degree of a testing system induces larger retrace errors demanding to be corrected. In the system based on the Twyman-Green interferometer, fringe frequency of the detected interferogram will be higher in a greater system non-null degree. Thus numerical experiments are executed in different non-null degrees with different maximum fringe frequencies of the interferogram to elaborate the retrace error correction results with the three methods. According to the Nyquist sampling principle, the maximum fringe frequency in the simulation is controlled to be less than 0.25 λ/pixel.

Transmission lens utilized here is an aplanat lens of *f*/2, producing a spherical wavefront with curvature radius of 270.9 mm. To achieve different system non-null degrees, Φ50 aspheres with different asphericity are tested with the nominal sag of the surface expressed as

$$z = \frac{cr^2}{1 + \sqrt{1 - (1 + k)c^2 r^2}} + \sum_{i=1}^{N} A_i r^{2i}, \tag{7}$$

where r is the radial coordinate of the asphere, k represents for the conic coefficient, c is the curvature of vertex, A_i is the coefficient of r^{2i} and N is the number of terms added to the conic base. Table 2 lists the aspheric prescription in this simulation with all test parts sharing the same conic base. In addition, to keep the comparability of the results, distribution of the actual figure error of all tested aspheres is the same as illustrated in Fig. 2(a), whose PV (peak-to-valley) is 0.5 λ and RMS (root-mean-square) is 0.07 λ.

To solve the figure error with the GDI method, deviation between the nominal aspheric shape and the spherical wavefront with curvature radius of 270.9 mm is subtracted from half of the corresponding wavefront on the image plane in each testing case. As for the TRW and ROR methods, the system is modeled with nominal shape of the tested asphere in each case for theoretical wavefront extraction and figure error reduction. Testing results after retrace error correction with the three methods in different non-null degrees (the maximum fringe frequency of the detected interferogram from 0 to 0.24 λ/pixel) are displayed in Fig. 2(b), showing the time consumption and RMS values of the residual

Table 2
Aspheric prescription. (a–l corresponding to the max. fringe freq. of 0.02–0.24 λ/pixel on the interferogram).

Conic base		$k=-1$		$c=1/270$		$A_1=0$	
No.		a	b	c	d	e	f
Coefficients	A_2	0	4.7e−9	6.5e−9	8.2e−9	9.8e−9	1.1e−8
	A_3	0	8.7e−14	1.08e−14	1.65e−14	1.04e−13	5.87e−13
No.		g	h	i	j	k	l
Coefficients	A_2	1.3e−8	1.4e−8	1.6e−8	1.8e−8	1.9e−8	2.1e−8
	A_3	2.12e−13	8.57e−13	4.44e−13	1.56e−14	5.99e−13	1.36e−13

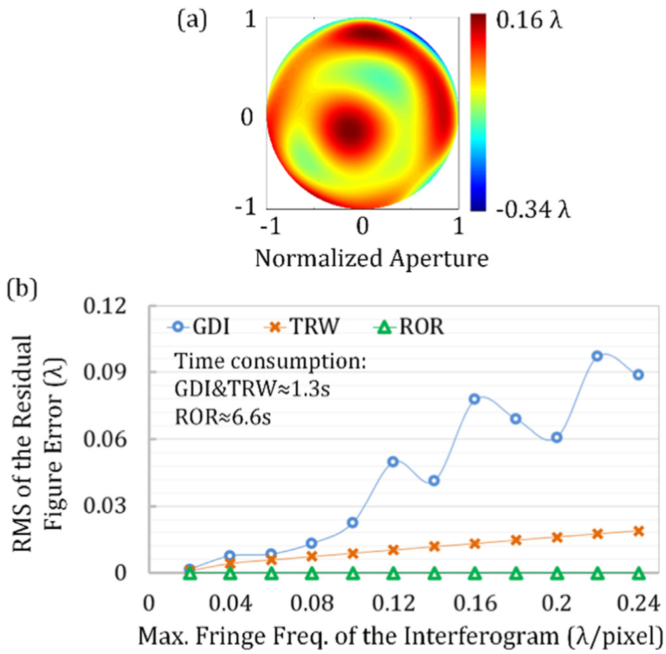

Fig. 2. (a) Distribution of the actual figure error (b) RMS of the residual figure error after retrace error correction with the GDI, TRW and ROR methods in different non-null degrees with the maximum fringe frequency of the interferogram from 0 to 0.24 λ/pixel.

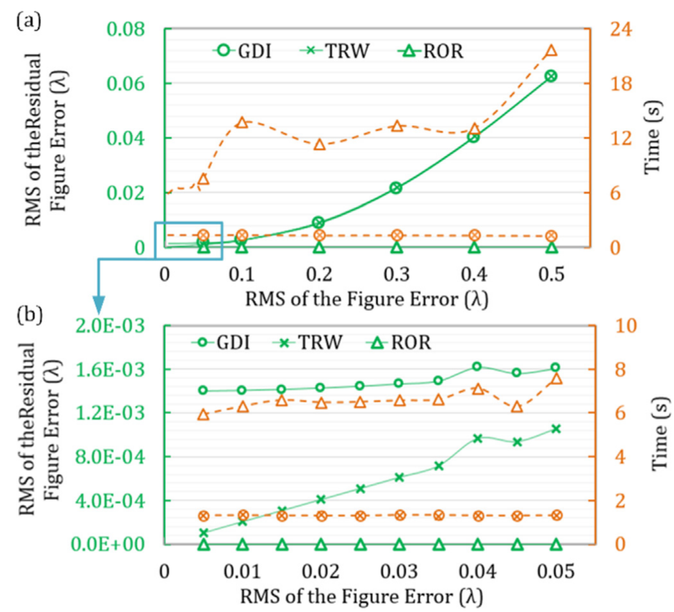

Fig. 3. Retrace error correction results of testing (a) figure errors from RMS=0.005 λ to 0.5 λ and (b) the detailed figure errors from RMS=0.005 λ to 0.05 λ in the system non-null degree with the maximum fringe frequency of 0.02 λ/pixel.

error between the reconstructed figure errors and the actual figure error. It can be seen that the GDI and TRW methods take much shorter time (about 1.3 s) for retrace error correction than the ROR method (about 6.6 s). However, these two methods lead to larger errors as the maximum fringe frequency (the system non-null degree) increases. Relation between the accuracy and the non-null degree is almost linear with the TRW method, while that of the GDI method has much to do with the high-order coefficients of the test part, or in other words the high-order aberrations. To achieve an accuracy of better than λ/100 RMS, the non-null degree of the system should be kept with the maximum fringe frequency of the detected interferogram less than 0.08 λ/pixel with the GDI method, and 0.12 λ/pixel with the TRW method respectively. While for the ROR method, testing results show that RMS of the residual figure error maintains in a magnitude of 10^{-6} λ. It is proved to be able to correct all the retrace errors caused by the non-null configuration theoretically, which is irrelevant to the non-null degree of the system. For the time consumption calculation here, we only count the time of retrace error correction and figure error reconstruction procedures. The computer employed for the calculation has four cores with the CUP frequency of 3.3 GHz and RAM of 3 GB.

3.2. Retrace error correction of testing different figure errors

From the above analyses, it is known that the GDI and TRW methods are fast in retrace error correction, but large non-null degrees leads to large errors. To guarantee the accuracy with these two methods, non-null degree of the testing system should be kept relatively low. However, besides non-null degree, testing accuracy is also affected by the unknown figure error, which also induces retrace error to the system. In order to understand to what range the figure error can be tested with acceptable accuracy in low non-null degree, numerical experiments are executed with the maximum fringe frequency of 0.02 λ/pixel in ideal conditions, to test figure errors from RMS=0.005 λ to 0.5 λ. Corresponding PV of these figure errors are from 0.05 λ to 5 λ. The distributions of the actual figure errors and the system prescription (including nominal shape of the test asphere, transmission lens) are the same as those of the first testing case in *Part 3.1*.

To correct the retrace error, the same deviation between the nominal aspheric shape and the spherical wavefront is subtracted from half of the corresponding wavefronts at the image plan in different testing cases with the GDI method. As for the TRW and ROR methods, the system model is the same in different testing cases since their difference is only the figure error to be tested. Therefore, theoretical wavefronts of the TRW method in these cases are also the same. Testing results of the time consumption and RMS of the residual figure errors with the three methods are displayed in Fig. 3 with respect to the tested figure errors. Although the non-null degree has been controlled as low as the maximum fringe frequency of 0.02 λ/pixel, retrace error correction with the GDI and TRW methods still induce more errors as the tested figure error becomes larger. It is shown in Fig. 3(a) that with the GDI and TRW methods, RMS of the residual figure error stays less than λ/200 in ideal conditions only when RMS of the tested figure error is less than 0.15 λ. In testing figure error larger than 0.2 λ RMS, results of the RMS error will be over λ/100. As for the ROR method, the RMS of the residual figure error still maintain in a magnitude of 10^{-6} λ, which keeps high accuracy in all testing cases. However, the time needed for retrace error correction with the ROR method increases from about 6.6 s to about 13.1 s and then to about 21.6 s as the enlargement of the tested figure error. In contrast, time consumption of the GDI and TRW algorithms keeps around 1.3 s unchangeably.

Considering the figure error around RMS = 0.05 λ can usually be achieved in precision optical elements manufacturing, Fig. 3 (b) details the results of testing figure errors from RMS = 0.005 λ to 0.05 λ. An accuracy of better than λ/500 RMS is achieved with the GDI and TRW methods in this case, but the error keeps larger with the GDI method than the TRW method. It is known from Fig. 3 (b) that for testing polished optics with RMS less than 0.05 λ in low system non-null degree, acceptable results can be achieved with all the three methods.

From Fig. 3 we can know that the testing error increases with the GDI and TRW methods as the tested figure error becomes larger. For relatively high accuracy, the figure error to be measured should be less than 0.2 λ RMS in low system non-null degree of 0.02 λ/pixel. As the system non-null degree increases, the system induced residual error becomes larger as mentioned above, leading to the upper limit of the aspheric figure error that can be tested decreases with the GDI and TRW methods. As for the ROR method, it corrects all the retrace errors accurately irrelevant to the tested figure error, but takes more time as the figure error becomes larger. To be noted, all the results are obtained in ideal emulational conditions.

3.3. Spherical vs. aspherical reference wavefront

The above numerical experiments are all executed with spherical reference wavefronts, which are commonly employed in non-null aspheric tests especially with the GDI method to facilitate the calculation. However, the dynamic range for testing a single aperture with spherical reference wavefront is limited as the asphericity of the test part increases.

Take concave parabolic mirrors with diameter of 100 mm and F number of 5, 2, 1.2 and 1.05 respectively as the test part for instance. Asphericity of the aspherics successively increases as the decreases of the F number. Best-fit spheres are employed as the incident test wavefronts for aspheric measurement and Fig. 4(a)–(d) shows the corresponding interferograms on the image plane. It is seen that Fig. 4(a) and (b) from the aspherics with F number of 5 and 2 are resolvable in the whole aperture, but fringe frequencies of (c) and (d) from testing aspherics with F number of 1.2 and 1.05 are too high to be recognized by the detector at one time. In this case, if the whole aperture aspheric is to be tested still with spherical wavefront, sub-apertures have to be divided. Testing the aspheres with F number of 1.2 and 1.05 in a single aperture at one time, the aspheric maximum diameter has to be reduced from 100 mm to 67 mm and 60 mm respectively (the maximum fringe frequency is controlled to be 0.08 λ/pixel).

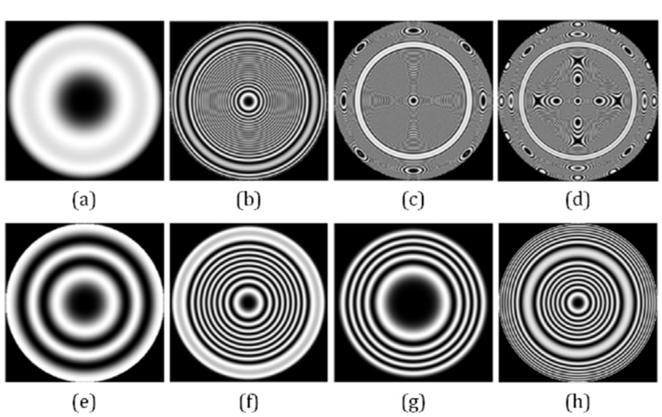

Fig. 4. (a)–(d) are interferograms of testing aspherics with F number of 5, 2, 1.2 and 1.05 respectively employing best-fit spherical wavefronts, (e)–(h) are the corresponding interferograms of testing the same aspherics employing aspherical wavefronts.

Table 3
Structure of the employed PCL.

Surface	Radius	Thickness	(Nd, Vd)	Semi-Diameter	Conic
1	89.148	10.6	(1.516780,	22.5	0
2	−50.678		64.28)	22.5	0

Fortunately, if we substitute the test wavefront from spherical to aspherical whose shape is more close to the test part, the dynamic range for aspheric testing can be enlarged and the non-null degree of the system can be better reduced. Fig. 4(e)–(h) shows the interferograms of testing the same aspheres corresponding to (a)–(d) with aspherical wavefronts. All the interferograms are able to be resolved in the whole aperture. Obviously, it is also acceptable to test aspherics with larger diameters in one single aperture.

To obtain the aspherical reference wavefront, a singlet lens (PCL, partial compensating lens) is employed as the transmission lens instead of an aplanatic lens which generates spherical wavefront. The structure of the PCL employed here is listed in Table 3.

With the singlet lens PCL, the system structure is much more simplified. Since an aplanatic lens contains at least three surfaces while PCL contains only two, errors induced by optics manufacturing and element calibration are reduced. In other words, not only the dynamic range is enlarged with aspherical wavefronts, but also the TRW and ROR methods are promoted fortunately, which need system modeling as accurate as possible for retrace error correction. Both the complexity of system calibration and the system modeling errors are reduced. Although aspherical wavefront is usually not employed in the GDI method for calculating complication, it is especially appropriate for the application of the TRW and ROR methods providing dynamic range enlargement and precision guarantee.

4. Experimental results

To illustrate the results, a Twyman-Green system shown as Fig. 1 with a frequency stabilized laser at wavelength of λ = 632.8 nm is set up to carry out the experiments. In the test arm, transmission lens is installed to transform the incident plane wave to the test wavefront. Since system modeling is required during the retrace error correction procedure with TRW and ROR methods, system modeling and calibration are implemented in advance by testing standard sphere to be coincident with the result obtained with Zygo phase-shifting Fizeau interferometer [24].

4.1. Experiments with spherical reference wavefront

In the experiment, a concave parabolic mirror with diameter of 158 mm and F number of 2.59 is tested. To correct retrace error with the GDI, TRW and ROR methods, spherical reference wavefronts are employed with an aplanatic lens as the transmission lens. As analyzed above, since the system non-null degree may also affect the testing results, two different non-null degrees are achieved to measure the same asphere by utilizing different reference spheres with curvature radius of 821.3 mm and 821.8 mm respectively. Fig. 5(a) and (b) shows the interferograms in these two cases, whose maximum fringe frequency is 0.06 λ/pixel and 0.10 λ/pixel respectively.

Retrace error is then corrected with the three methods separately in the two system non-null degrees. Fig. 5(c) and (d) displays the testing results obtained from interferograms shown in Fig. 5(a) and (b) respectively with the GDI method,

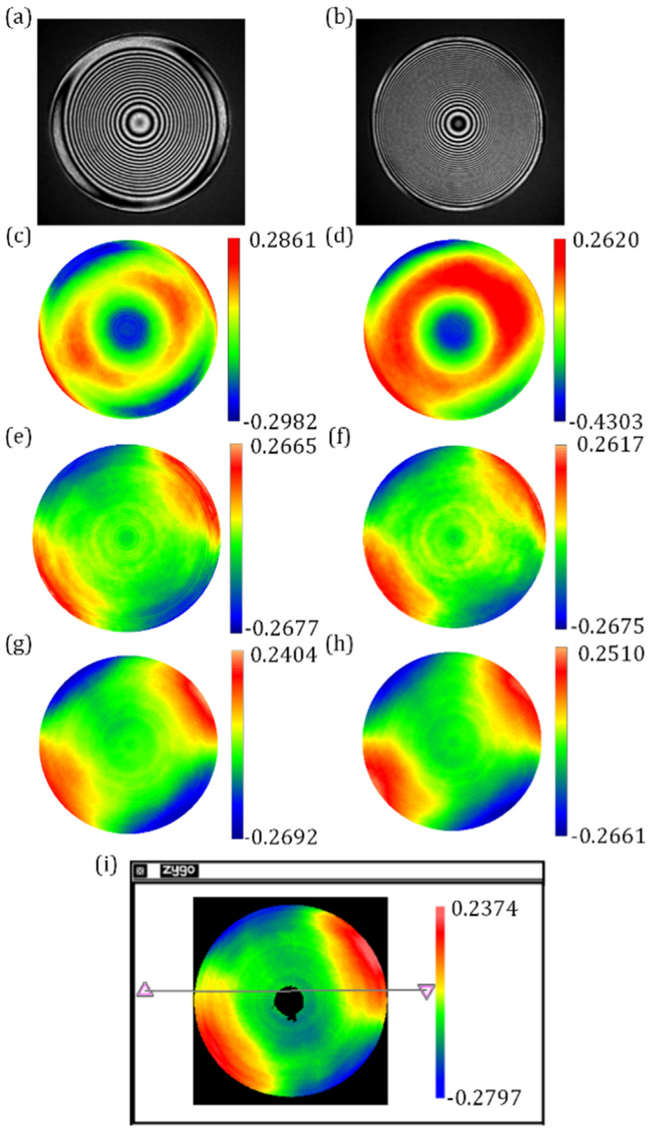

Fig. 5. (a) and (b) are interferograms detected with spherical reference wavefronts in the non-null degree with the maximum fringe frequency of 0.06 λ/pixel and 0.10 λ/pixel respectively, (c) and (d) are the corresponding results obtained with the GDI method in the case of (a) and (b), (e) and (f) are results with the TRW method, (g) and (h) are those with the ROR method, (i) is the result obtained with the autocollimation method for contrast. (unit: λ).

Table 4
PV and RMS values of the testing results. (unit: λ).

Maximum fringe frequency	Method	PV	RMS
0.06 λ/pixel	GDI	0.5843	0.1093
	TRW	0.5342	0.0743
	ROR	0.5096	0.0889
0.10 λ/pixel	GDI	0.6923	0.1452
	TRW	0.5292	0.0716
	ROR	0.5171	0.0878
–	Null	0.517	0.091

(e) and (f) shows the results obtained with the TRW method, while (g) and (h) are the results obtained with the ROR method. For contrast, the same aspheric is tested employing the autocollimation null testing method with Zygo GPI interferometer and Fig. 5 (i) shows the figure error result.

It is seen that large retrace errors are still left in Fig. 5(c) and (d) with the GDI method. Since the test asphere has relatively large aperture and figure error with smaller F number, it is hard to correct the retrace error to an acceptable extent in both non-null degrees. As the system non-null degree becomes higher, the results deviate more from the null test. Fig. 5(e) and (f) shows the results obtained with the TRW method, which illustrate more similar topographic maps to (i) than (c) and (d). As for the ROR method, better consistency to the null test is shown in (g) and (h). To further evaluate the testing results, PV and RMS values of each test are listed in Table 4. For the TRW and ROR methods, the results are considered to be stable in the two system non-null degrees with RMS errors of the TRW method around λ/50 and those of the ROR method less than λ/200. While for the GDI method, the RMS error increases as the system non-null degree becomes larger. The results are agreed with the numerical analyses above. To be noted, since the autocollimation method misses the center part information of the test aspheric and its accuracy is also affected by many factors, the testing result of (i) only provides a hint for the comparison.

4.2. Experiments with aspherical reference wavefront

Dynamic range of testing a single aperture with spherical wavefront is very limited as the increase of the asphericity of the test part. For example, in the test of a concave parabolic mirror with diameter of 101 mm and F number of 1.19, if spherical wavefront is still employed, the fringes on the detected interferogram will be too dense to be resolved over the full aperture as shown in Fig. 6 (a). Sub-apertures have to be divided and tested separately to obtain the whole aperture result with stitching procedure. To test the full aperture aspheric at one time, PCL detailed in Table 3 is substituted to the aplanat lens as the transmission lens providing aspherical wavefront for the testing. Fig. 6(b) and (c) displays the interferograms detected in this case. The maximum fringe frequency of each interferogram is 0.025 λ/pixel and 0.045 λ/pixel respectively achieved by altering the location of the test part..

Since the reference wavefront is aspherical, retrace error is therefore corrected with the TRW and ROR methods separately. Fig. 7(a) and (b) display the testing results obtained with the TRW method in the two different non-null degrees shown as Fig. 6 (b) and (c), while those of the ROR method are displayed in Fig. 7 (c) and (d). For contrast, the same asphere is also tested employing the autocollimation method with Zygo GPI interferometer. Fig. 7 (e) shows the null test result.

From Fig. 7, it is seen that when testing an asphere with figure error around 0.3 λ PV, both TRW and ROR methods are able to illustrate acceptable results similar to the null test in the system

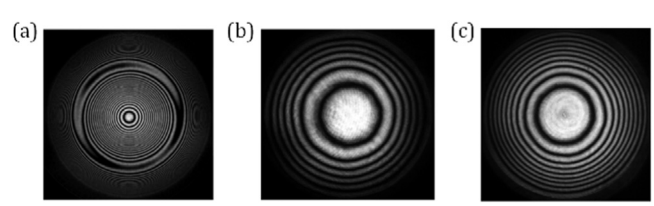

Fig. 6. (a) is the interferogram detected with spherical reference wavefront, (b) and (c) are interferograms detected with aspherical reference wavefronts in the non-null degree with the maximum fringe frequency of 0.025 λ/pixel and 0.045 λ/pixel respectively.

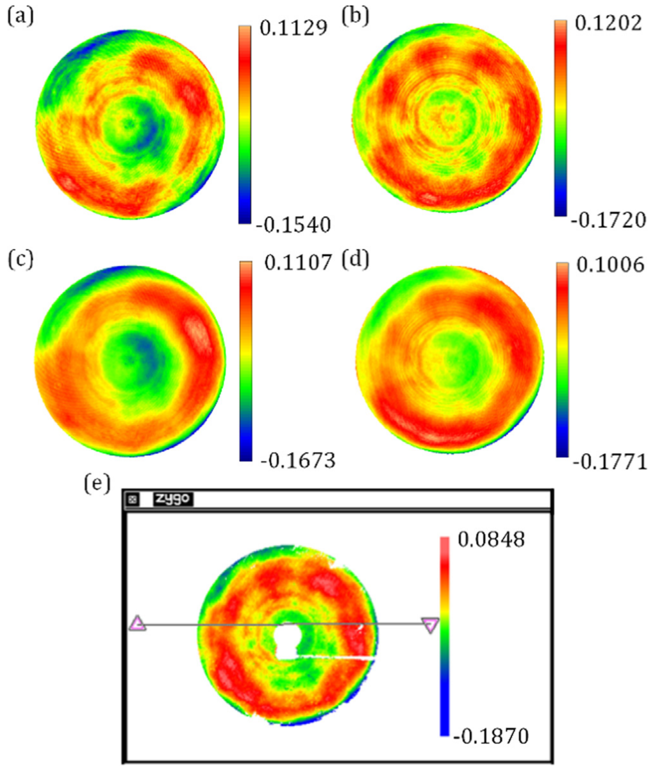

Fig. 7. (a) and (b) are testing results with the TRW method in different system non-null degrees of Fig. 6(b) and (c) with the maximum fringe frequency of 0.025 λ/pixel and 0.045 λ/pixel respectively, (c) and (d) are the corresponding results obtained with the ROR method, (e) is the result obtained with the autocollimation method. (unit: λ).

Table 5
PV and RMS values of the testing results. (unit: λ).

Maximum frequency	Method	PV	RMS
0.025 λ/pixel	TRW	0.2669	0.0379
	ROR	0.2782	0.0331
0.045 λ/pixel	TRW	0.2922	0.0304
	ROR	0.2777	0.0364
–	Null	0.272	0.035

non-null degrees of less than 0.05 λ/pixel. Consistency of the topographic maps is kept well to the null test result with both methods in this case and the result also agrees with the numerical analyses above. Table 5 lists the PV and RMS values of these tests. Errors between the non-null tests and the null test are very small.

To be noted, since the algorithms of the GDI and TRW methods employ point to point calculation, they are sensitive to the environment noise in practical measurements. This noise influence can be restrained by environment control and high frequency filtering of the detected wavefront. On the other hand, adjusting accuracy also affects the results. In most cases, the position error tolerance of the test part within a 10 μm decentration, 10 s tilt and 15 μm defocus is acceptable.

5. Discussion and conclusions

Retrace error correction in non-null aspheric testing is essential which directly affects the accuracy of the testing results. Three practical retrace error correction methods for non-null aspheric testing are analyzed for the testing of a single circular aperture. Dynamic range of these methods (applicable non-null degrees, figure error scale, time consumption, et al.) are sought out to guide practical application. Although the figure error distribution employed in the simulation is specific, different distributions with the same RMS values share similar testing accuracy and tendency. General comparative results are concluded in Table 6.

Table 6
Comparative results of the three methods.

Evaluation items	GDI	TRW	ROR
System Modeling	No	Yes	Yes
Reference Wavefront	Spherical	Either spherical or aspherical	
Non-null Degree	Max fringe frequency < 0.05 λ/pixel		Within resolution
Figure Error	RMS < 0.07 λ	RMS < 0.07 λ	Within resolution
Residual Error	Larger than ROR	Larger than ROR	Small
Time Consumption	≈ 1 s	≈ 1 s	6–20 s
Applied to Sub-Apertures	Yes	Yes	Yes

With the GDI and TRW methods, more errors will be induced as the tested figure error or the system non-null degree increases. The scale of the tested figure error depends on the system non-null degree and high-order aberrations affects more to the GDI method. As for the ROR method, the asphere is able to be tested as long as the interferogram is resolvable. Moreover, it is proposed that by employing aspherical reference wavefront, the dynamic range can be further enlarged. Especially in subaperture stitching tests, subaperture number with aspherical reference wavefront is usually less than that with a spherical one [6]. With PCL to simplify the system structure for aspherical wavefront generating, the calibration work and system modeling error is reduced and promotes the application of the TRW and ROR methods.

Due to the properties of large dynamic range, less structure alteration for different aspherics and high accuracy, the ROR method is recommended for commercial instruments and research works. While the GDI and TRW methods are more appropriate for fast tests of apertures with small figure error in low system non-null degrees.

Acknowledgments

This work was partially supported by the National Key Research and Development Program of China [2016YFC0200704]; the National Natural Science Foundation of China [41305014, 61475141]; the State Key Laboratory of Applied Optics open funds.

References

[1] John E. Greivenkamp, Sub-Nyquist interferometry, Appl. Opt. 26 (1987) 5245–5258.
[2] D. Liu, Y. Yang, C. Tian, Y. Zhuo, Partial null lens for general aspheric testing, Infrared Laser Eng. 38 (2009) 322–325.
[3] P. Murphy, G. Forbes, J. Fleig, P. Dumas, M. Tricard, Stitching interferometry: a flexible solution for surface metrology, Opt. Photonics News 14 (2003) 38–43.
[4] Y.M. Liu, G.N. Lawrence, C.L. Koliopoulos, Subaperture testing of aspheres with annular zones, Appl. Opt. 27 (1988) 4504–4513.
[5] S. Chen, C. Zhao, Y. Dai, S. Li, Reconfigurable optical null based on counter-rotating Zernike plates for test of aspheres, Opt. Express 22 (2014) 1381–1386.
[6] L. Zhang, C. Tian, D. Liu, T. Shi, Y. Yang, H. Wu, Y. Shen, Non-null annular subaperture stitching interferometry for steep aspheric measurement, Appl. Opt. 53 (2014) 5755–5762.
[7] E. Garbusi, C. Pruss, W. Osten, Interferometer for precise and flexible asphere testing, Opt. Lett. 33 (2008) 2973–2975.
[8] J. Schwider, N. Lindlein, K. Mantel, I. Harder, On the calibration of diffractive nulls for transmission tests of aspheric components, Opt. Commun. 279 (2007)

262–272.
[9] D. Liu, Y. Yang, C. Tian, Y. Luo, L. Wang, Practical methods for retrace error correction in nonnull aspheric testing, Opt. Express 17 (2009) 7025–7035.
[10] R.O. Gappinger, J.E. Greivenkamp, Iterative reverse optimization procedure for calibration of aspheric wave-front measurements on a nonnull interferometer, Appl. Opt. 43 (2004) 5152–5161.
[11] C. Huang, Propagation errors in precision Fizeau interferometry, Appl. Opt. 32 (1993) 7016–7021.
[12] C.J. Evans, Compensation for errors introduced by nonzero fringe densities in phase-measuring interferometers, Ann. CIRP 42 (1993) 577–580.
[13] P.E. Murphy, T.G. Brown, D.T. Moore, Measurement and calibration of interferometric imaging aberrations, Appl. Opt. 39 (2000) 6421–6429.
[14] X. Wang, Test on large convex aspherical mirror by subaperture stitching interferometry, Infrared Laser Eng. 42 (2013) 716–722.
[15] E. Garbusi, W. Osten, Perturbation methods in optics: application to the interferometric measurement of surfaces, J. Opt. Soc. Am. A 26 (2009) 2538–2549.
[16] G. Baer, J. Schindler, C. Pruss, J. Siepmann, W. Osten, Calibration of a non-null test interferometer for the measurement of aspheres and free-form surfaces, Opt. Express 22 (2014) 31200–31211.
[17] Y. He, X. Hou, H. Quan, W. Song, Retrace error reconstruction based on point characteristic function, Opt. Express 23 (2015) 28216–28223.
[18] C. Tian, Y. Yang, Y. Zhuo, Generalized data reduction approach for aspheric testing in a non-null interferometer, Appl. Opt. 51 (2012) 1598–1604.
[19] A.E. Lowman, J.E. Greivenkamp, Modeling an interferometer for non-null testing of aspheres, Proc. SPIE 2536 (1995) 139–147.
[20] D. Liu, T. Shi, L. Zhang, Y. Yang, S. Chong, Y. Shen, Reverse optimization reconstruction of aspheric figure error in a non-null interferometer, Appl. Opt. 53 (2014) 5538–5546.
[21] H. Kurita, Interferometric Aspheric Surface Testing Using Ray Tracing Code, University of Arizona, Tucson, Arizona, 1989.
[22] J.D. Micali, J.E. Greivenkamp, Method for reconstruction of complex surface shapes from a reflection-based non-null interferometric measurement, Opt. Eng. 55 (2016) 034101.
[23] Z. Gao, L. Chen, R. Zhu, Computer-aided alignment for a reference transmission sphere of an interferometer, Opt. Eng. 43 (2004) 69–74.
[24] L. Zhang, D. Liu, T. Shi, Y. Yang, S. Chong, B. Ge, Y. Shen, J. Bai, Aspheric subaperture stitching based on system modeling, Opt. Express 23 (2015) 19176–19188.
[25] H. Liu, Z. Lu, F. Li, Y. Xie, Q. Sun, Testing aspheric in interferometric setups: removal of adjustment errors from measurement result, Opt. Commun. 242 (2004) 339–344.
[26] L. Zhang, D. Liu, T. Shi, Y. Yang, Y. Shen, Practical and accurate method for aspheric misalignment aberrations calibration in non-null interferometric testing, Appl. Opt. 52 (2013) 8501–8511.